## NEUROSCIENCE

# Depolarization block in olfactory sensory neurons expands the dimensionality of odor encoding

David Tadres[1,2], Philip H. Wong[1,3], Thuc To[1], Jeff Moehlis[3], Matthieu Louis[1,4]*

Upon strong and prolonged excitation, neurons can undergo a silent state called depolarization block that is often associated with disorders such as epileptic seizures. Here, we show that neurons in the peripheral olfactory system undergo depolarization block as part of their normal physiological function. Typically, olfactory sensory neurons enter depolarization block at odor concentrations three orders of magnitude above their detection threshold, thereby defining receptive fields over concentration bands. The silencing of high-affinity olfactory sensory neurons produces sparser peripheral odor representations at high-odor concentrations, which might facilitate perceptual discrimination. Using a conductance-based model of the olfactory transduction cascade paired with spike generation, we provide numerical and experimental evidence that depolarization block arises from the slow inactivation of sodium channels—a process that could affect a variety of sensory neurons. The existence of ethologically relevant depolarization block in olfactory sensory neurons creates an additional dimension that expands the peripheral encoding of odors.

## INTRODUCTION

Animals detect odors through a repertoire of odorant receptors that are selectively expressed in olfactory sensory neurons (OSNs). In most vertebrates and insects, the peripheral representation of odors relies on the combinatorial activation of OSNs: While each odor activates a different ensemble of OSNs, most OSNs are activated by more than one odor (*1–3*). The dose response of any OSN is believed to follow a sigmoidal function that grows monotonically until it reaches a plateau (*4–10*). Hence, increasingly larger fractions of OSNs are expected to be active at higher-odor concentrations, which might undercut the ability to efficiently discriminate between similar odors (*11*).

Here, we show that OSNs stimulated for several seconds by high concentrations of their high-affinity odors can undergo a state of depolarization block, which abolishes their normal spiking activity. As a consequence of the silencing of OSNs that undergo strong olfactory transduction currents, high-odor concentrations do not necessarily recruit increasingly large numbers of OSNs. Together, our results indicate that depolarization block fulfills an important physiological function in sensory neurons besides its involvement in disease states such as epilepsy (*12, 13*) and migraines (*14*).

## RESULTS

### OSNs undergo depolarization block when stimulated by ethologically relevant odor concentrations

Fruits that are attractive to *Drosophila melanogaster* emit complex blends of odorant molecules that include esters detected by the *Or42b*-expressing OSNs (*15*). When exposed to a piece of ripe banana, wild-type larvae quickly locate the source of the odor through directed navigation (Fig. 1, A to C; fig. S1A; and movie S1), as shown in previous work with pure odors (*16–19*). A markedly different behavior was observed in larvae with olfactory inputs limited to a single OSN by selectively rescuing the expression of the odorant co-receptor ORCO in the *Or42b* OSN of anosmic *Orco* null (*Orco*$^{-/-}$) mutant larvae (*20*) (see Materials and Methods). Instead of locating and readily entering the piece of banana, *Or42b* single functional (*Or42b* SF) larvae circled at an intermediate distance to the source between the full attraction of wild type and the nonattraction of anosmic larvae (Fig. 1, B and C). Using an assay where the odor diffusion can be quantified in gaseous phase (*17*) and modeled numerically (*21*), we established that wild-type larvae are attracted to ethyl butyrate—a fruity ester released by ripe banana (*15, 22*)—over a relatively wide range of concentrations (Fig. 1, D to F). By contrast, *Or42b* SF larvae were repelled by the odor source at high strengths (1:150 and 1:100 source dilutions, see Materials and Methods for details) that are strongly attractive to wild-type larvae (Fig. 1, E and F). To confirm this unexpected result, we developed a genetic strategy to inhibit synaptic transmission in all OSNs except the *Or42b* OSN through selective expression of the tetanus toxin light chain (TNT) (fig. S1F) (*23*). As for the regular *Or42b* SF larvae, we observed that larvae with all but their *Or42b* OSNs functionally impaired are repelled by a source of ethyl butyrate at high strength (fig. S1, F and G).

To define the basis of the concentration-specific attraction mediated by the *Or42b* OSN, we used suction electrode recordings (Fig. 2A) to monitor the activity of the *Or42b* OSN in response to (i) prolonged odor step stimuli at fixed concentrations (Fig. 2, C and D, and fig. S1H) and (ii) replays of the time courses of odor concentration experienced by the freely moving larvae in gradients of ethyl butyrate (Fig. 2, E and F). For an attractive source dilution (1:7.5×10$^3$), the *Or42b* OSN showed robust firing activity throughout the concentration range of the replay (0.4 to 1 μM; see Fig. 2E; fig. S1, I and J; and Materials and Methods for details about concentration replays). Consistent with the response properties of the larval *Or42a* OSN stimulated by dynamic odor profiles (*21*), the *Or42b* OSN tracked and amplified changes in odor concentration.

[1]Department of Molecular, Cellular, and Developmental Biology and Neuroscience Research Institute, University of California, Santa Barbara, Santa Barbara, CA, USA. [2]Department of Molecular Life Sciences, University of Zurich, Zurich, Switzerland. [3]Department of Mechanical Engineering, University of California, Santa Barbara, Santa Barbara, CA, USA. [4]Department of Physics, University of California, Santa Barbara, CA, USA.
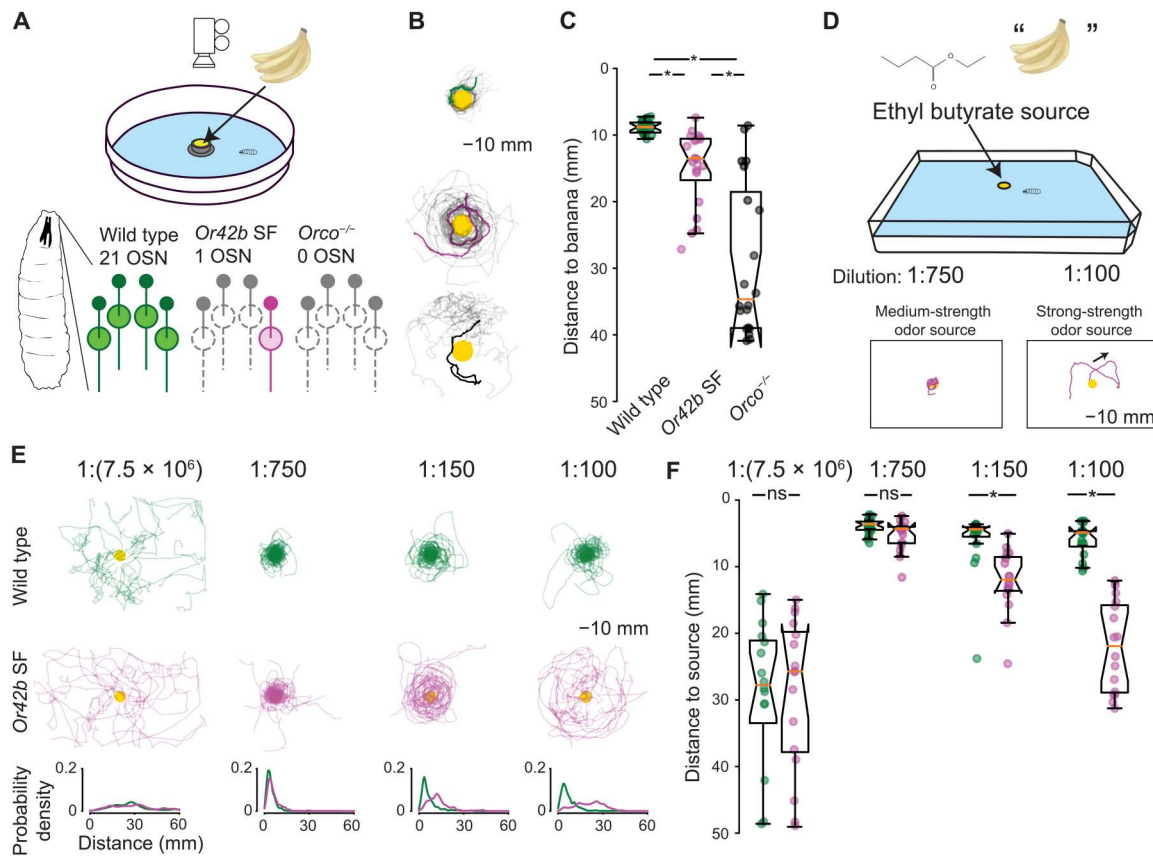*Corresponding author. Email: mlouis@ucsb.edu

**Fig. 1. *Drosophila* larvae with a single OSN are attracted to a food source but unable to reach it.** (**A**) Schematic of banana olfaction assay (top). Schematic of larval olfactory systems with full and genetically-manipulated functionality (bottom). (**B**) Trajectories produced by wild type (top), *Or42b* SF (middle), and anosmic *Orco* null (*Orco*$^{-/-}$) mutant (bottom). The yellow disk indicates position of the fruit cup. (**C**) Quantification of distance to cup of wild type (green, $n = 20$), *Or42b* SF (magenta, $n = 20$), and *Orco*$^{-/-}$ mutant (gray, $n = 20$). Statistical differences between genotypes were tested using Kruskal-Wallis H test, followed by Conover-Iman test (*$P < 0.05$). (**D**) Schematic of assay featuring a single odor source (top). Illustrative trajectories of *Or42b* SF in response to an ethyl butyrate source of medium (1:750) and strong (1:100) strengths. (**E**) Trajectories produced by wild-type (top) and *Or42b* SF (middle) larvae at the indicated source dilutions of ethyl butyrate. Probability density functions of distance to source (bottom) for wild type (green) and *Or42b* SF (magenta). (**F**) Pairwise comparisons between wild-type and *Or42b* SF behaviors using Wilcoxon rank sum test (*$P < 0.05$ upon Bonferroni correction). See data S1 for $P$ values. ns, not significant.

The OSN dynamics markedly differed for a stronger odor source (1:150) that elicited behavioral aversion: When stimulated by high-odor concentrations that initially induced strong excitation (>10 μM; Fig. 2F), the *Or42b* OSN switched from sustained firing activity to a silent state reminiscent of depolarization block (see below).

For prolonged odor stimulation at fixed concentrations, the firing activity associated with the initial phasic response of the *Or42b* OSN produced a canonical sigmoidal dose response (Fig. 2B, dark blue trace), as reported in previous work (*9*). While the firing activity was maintained throughout the 20-s stimulation at odor concentrations lower than 10 μM (Fig. 2C), the tonic response of the *Or42b* OSN switched to a block state at concentrations higher than 10 μM (Fig. 2, B, cyan trace and red arrow, and D). Even for stimuli of high-odor concentrations, several seconds were necessary for the OSN dynamics to evolve toward depolarization block (fig. S1H). However, once developed, the block state persisted throughout the rest of the 20-s odor stimulation.

## Depolarization block does not arise from inhibition of the olfactory transduction cascade

In the adult *Drosophila*, a feedback loop involving the inhibitory effect of intracellular calcium on the activity of the odorant receptor adaptively regulates the olfactory transduction cascade (*24*, *25*). In the larva, modeling suggests that a similar negative feedback contributes to the regulation of the odor-driven activity of the *Or42a* OSN (*21*), but such feedback is not expected to influence the OSN activity induced optogenetically (*20*). To test whether the depolarization block of the *Or42b* OSN stems from a similar negative feedback regulation of the olfactory transduction cascade, we characterized the olfactory behavior of *Or42b* SF larvae expressing the light-gated cation channel ChrimsonR (*Or42b>Chrimson*; Fig. 3, A and B) (*26*). For a source of ethyl butyrate at medium strength (1:750), *Or42b>Chrimson* larvae displayed vigorous attraction (Fig. 3, C and D, left). When combining an odor source of the same strength with a concentric red light gradient, *Or42b>Chrimson* larvae displayed repulsion (Fig. 3, C and D, right). We used suction electrode recordings to characterize the response of the *Or42b>Chrimson* OSN stimulated by brief light flashes
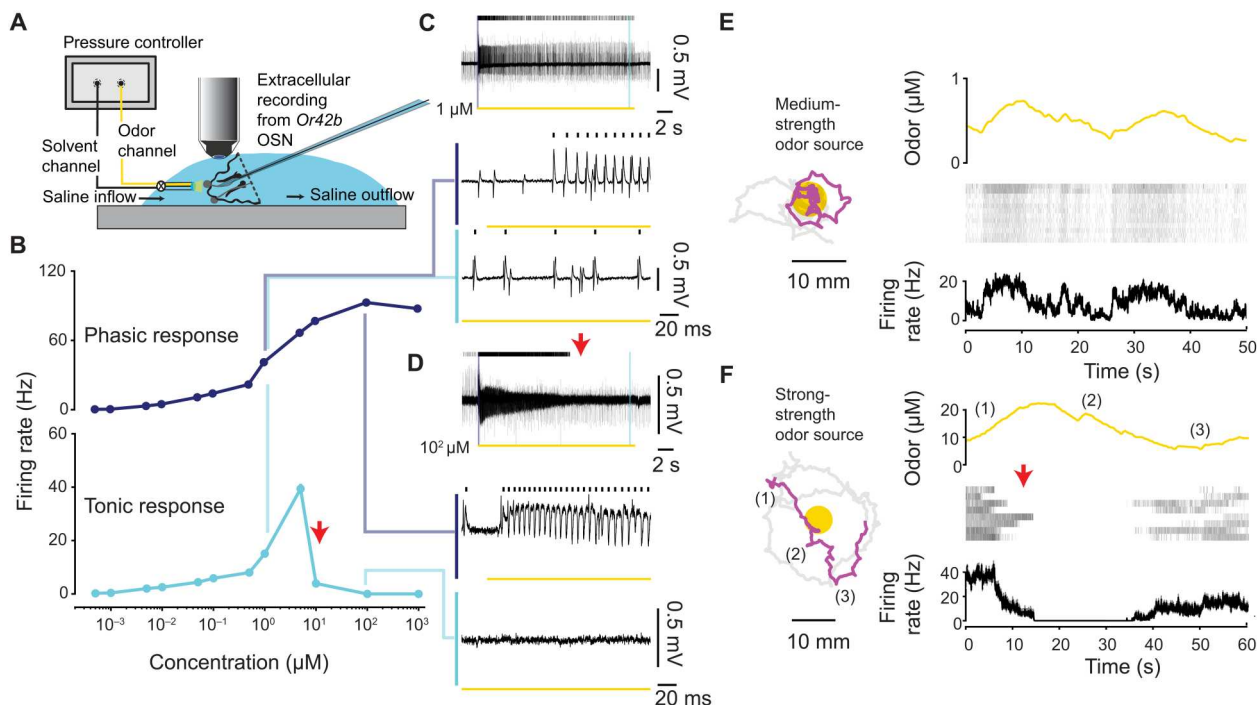
**Fig. 2. OSNs undergo depolarization block during chemotaxis.** (**A**) Schematic of olfactometer and electrophysiology setup. (**B**) Phasic (top) and tonic (bottom) dose-response profiles of *Or42b* OSN to ethyl butyrate. Data represent mean firing rates ± SEM (500 pM, *n* = 10; 1 nM, *n* = 10; 5 nM, *n* = 10; 10 nM, *n* = 10; 50 nM, *n* = 18; 100 nM, *n* = 18; 1 μM, *n* = 10; 5 μM, *n* = 8; 10 μM, *n* = 9; 100 μM, *n* = 10; and 1 mM, *n* = 10). (**C**) Representative recording of *Or42b* OSN stimulated by 1 μM ethyl butyrate. Raster plot shows the OSN-specific spikes (top). Yellow line below indicates 20-s odor stimulation; thin blue and cyan lines indicate "phasic response" and "tonic response," respectively. (**D**) Same as (C) for *Or42b* OSN at 100 μM. (**E**) Replay of concentration time course corresponding to a trajectory segment (magenta) obtained for a medium-strength source (1:7.5×10³, *n* = 12). (**F**) Same as (E) for strong-strength source (1:150, *n* = 8). Red arrow in (D) and (F) indicates onset of depolarization block.

superimposed onto a step stimulus of ethyl butyrate. For a medium concentration of ethyl butyrate (100 nM and 1 μM), the light flashes elicited reproducible spike trains (Fig. 3E). For a high-odor concentration (100 μM) inducing depolarization block, the light flashes did not produce action potentials (Fig. 3E). Together, these results indicate that depolarization block of the *Or42b* OSN can be caused by currents originating either from the odorant receptor or from Chrimson, which rules out an inhibitory mechanism that selectively targets the olfactory transduction cascade.

**Depolarization block is commonly observed in larval OSNs**
Next, we asked whether depolarization block can be induced in olfactory neurons other than the *Or42b* OSN. To this end, the OR42b receptor was ectopically expressed in the *Or1a* OSN (Fig. 3F), a neuron that normally has a low sensitivity to ethyl butyrate (*9*). Larvae directed by the endogenous single functional *Or1a* OSN displayed attraction to a very strong (1:25) but not a medium (1:750) source of ethyl butyrate (Fig. 3G, blue, and fig. S2A). Upon ectopic expression of OR42b in the *Or1a* OSN (*Or1a>Or42b* SF), the attraction observed for the very strong (1:25) source of ethyl butyrate was converted into repulsion (Fig. 3, G and H, magenta). In suction electrode recordings, the wild-type *Or1a* OSN responded with substantial firing activity to both low and high concentrations of ethyl butyrate (10² and 10⁴ μM; Fig. 3I). Upon ectopic expression of OR42b in the *Or1a* OSN, the *Or1a>Or42b* OSN was strongly activated by low concentrations of ethyl butyrate but underwent depolarization block in the tonic phase when presented with high-odor

concentrations (10⁴ μM; Fig. 3I, red arrow). Therefore, the high conductance of OR42b gated by one of its high-affinity ligands (*3*, *27*) was sufficient to induce depolarization block in an OSN that had an endogenously low affinity to the same odor. This result suggested that any OSN excited by strong transduction currents can switch to a block state.

To establish the relevance of depolarization block for different ligand-odorant-receptor pairs, we selected 4-hexen-3-one—a fruity-smelling ketone with a high affinity for the OR42a odorant receptor (Fig. 4A) (*9*). While strong attraction was observed in *Or42a* SF larvae at a source of medium strength (1:9×10⁴), strong aversion was triggered by a stronger source (1:9×10²) (Fig. 4, B and C). Larvae followed concentration isoclines—they circled—around a strong source of 4-hexen-3-one, driven by the attraction to the odor at low concentrations and its aversion at high concentrations (Fig. 4B). Electrophysiological recordings of the *Or42a* OSN revealed that depolarization block is elicited at high concentrations of 4-hexen-3-one (Fig. 4D, red arrow). Next, we generalized the relevance of depolarization block to a third odorant receptor, OR13a, which recognizes the fruity ester pentyl acetate (Fig. 4E) (*3*). While *Or13a* SF larvae are attracted by a source of pentyl acetate at medium strength (1:7×10²), the same larvae are repelled by a stronger (1:23) source (Fig. 4, F and G). Behavioral aversion correlated with the onset of depolarization block when the *Or13a* OSN was stimulated by a high concentration of pentyl acetate (Fig. 4H, red arrow). For all conditions that elicited repulsion at high-odor concentrations leading to circling behavior in single
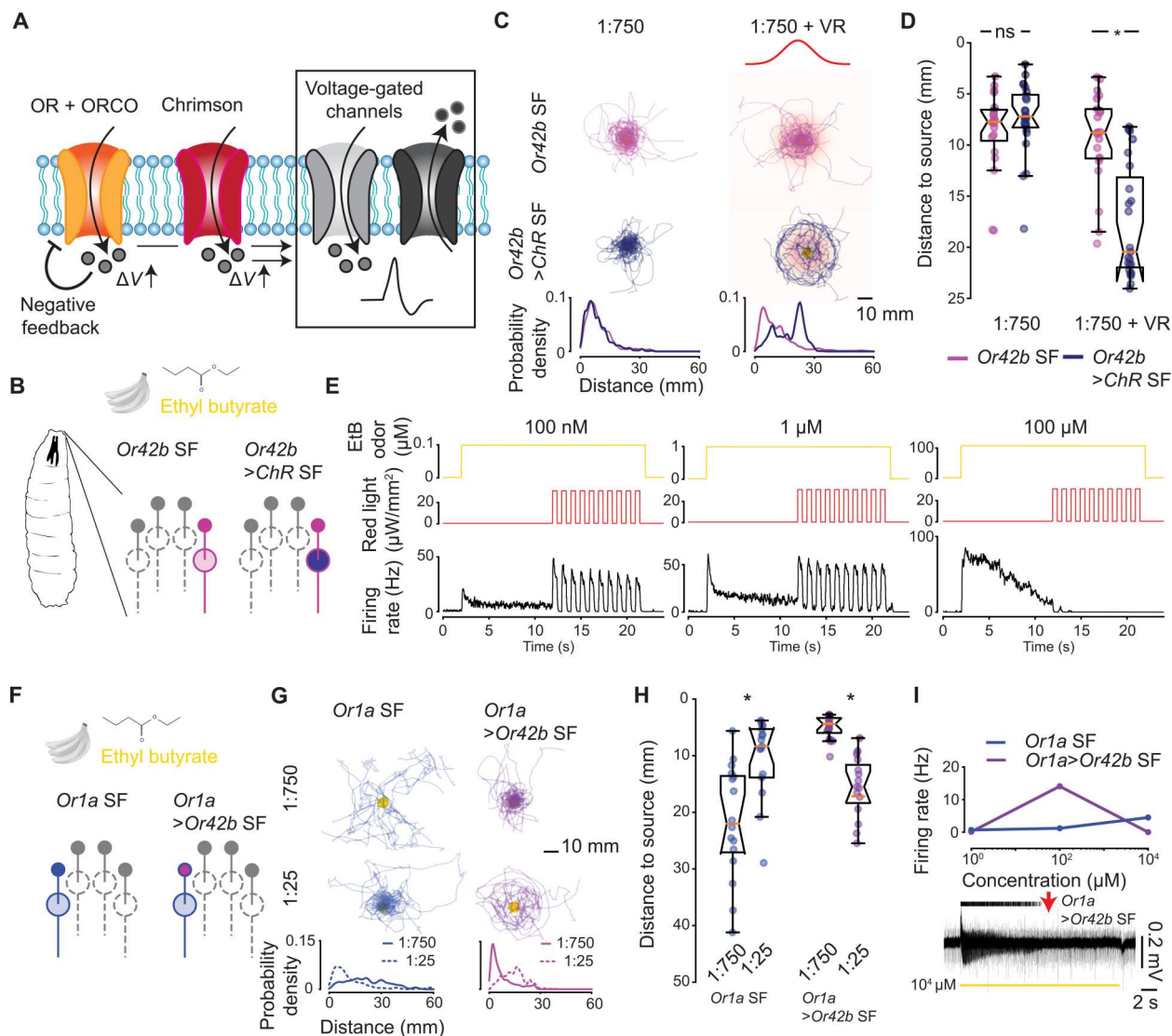
**Fig. 3. Depolarization block is a property of OSNs.** (**A**) The light-gated cation channel ChrimsonR (red, ChR) is used to test whether the negative feedback involved in regulating the olfactory transduction cascade (orange) is necessary for depolarization block (*24*, *25*). (**B**) Expression of ChrimsonR in the *Or42b* OSN. (**C** and **D**) No difference in attraction level was observed between *Or42b* SF (*n* = 20) and *Or42b>ChR* SF (*n* = 23) without light stimulation. For animals exposed to a virtual light gradient superimposed onto an ethyl butyrate (1:750) gradient, *Or42b>ChR* SF (*n* = 23) is repelled by the gradient peak compared to *Or42b* SF (*n* = 21) (Wilcoxon rank sum test, *P* < 0.05 upon Bonferroni correction). VR denotes a virtual light gradient with a peak light intensity of 41 μW/mm². (**E**) PSTH of *Or42b>ChR* OSN elicited by prolonged stimulus of ethyl butyrate at a concentration of 100 nM (left, *n* = 12), 1 μM (middle, *n* = 10), and 100 μM (right, *n* = 10) with red light flashes of 0.5 s. When the *Or42b* OSN has undergone depolarization block (right), red light flashes fail to elicit action potentials. (**F**) Ectopic expression of OR42b in the *Or1a*-expressing OSN. (**G** and **H**) *Or1a* SF is significantly less attracted to low-strength (1:750, left, *n* = 16) than high-strength (1:25, right, *n* = 17) sources. Following the ectopic expression of OR42b in *Or1a* SF, larvae become repelled at high-strength source (1:25, *n* = 15) compared to medium-strength source (1:750, *n* = 16). Wilcoxon rank sum test (*P* < 0.05 upon Bonferroni correction). (**I**) Top: Mean ± SEM tonic firing rates recorded from *Or1a* OSN (1 μM, *n* = 10; 10² μM, *n* = 11; and 10⁴ μM, *n* = 10) and for *Or1a>Or42b* OSN (1 μM, *n* = 10; 10² μM, *n* = 10; and 10⁴ μM, *n* = 10). Bottom: Representative voltage traces. Red arrow indicates onset of depolarization block. Raster plot reports the OSN-specific spikes, and yellow bar indicates timing of odor stimulation. The bottom row of (C) and (G) shows the probability density functions of distance to source. See data S1 for *P* values.

functional OSN larvae, we verified that wild-type larvae displayed strong attraction, whereas anosmic larvae showed no signs of attraction (fig. S2).

## A computational model elucidates the mechanistic origin of depolarization block in OSNs

In dopamine neurons of the midbrain of rats, depolarization block is mediated by the cumulative effects of slow inactivation of the voltage-gated sodium channels (*28*). Given that the depolarization block affecting an OSN does not appear to be caused by negative regulation of the olfactory transduction cascade (Fig. 3, A to E), we speculated that the block of OSNs resulted from the inhibition of sodium channels associated with the spike generation machinery. In *Drosophila*, voltage-gated sodium channels are thought to be the products of complex patterns of alternative splicing of a single gene called *paralytic* (*29*, *30*). As described in Fig. 5 (A and B), we
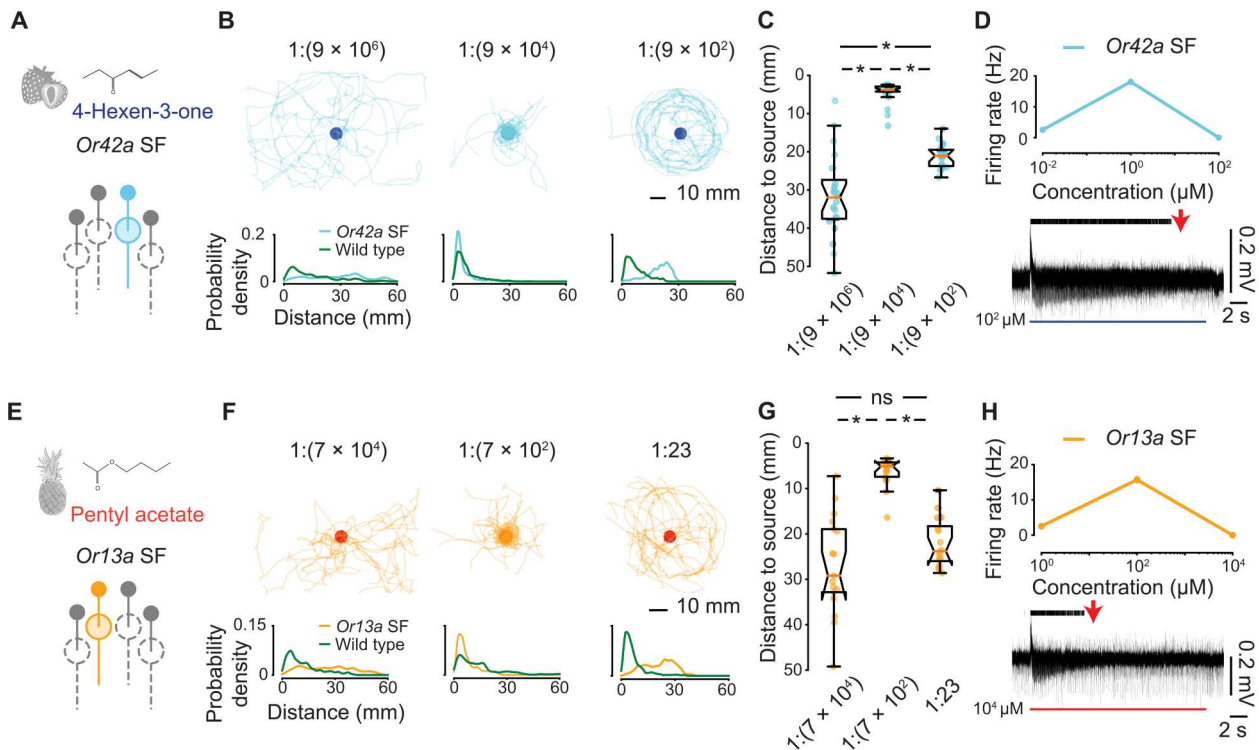
**Fig. 4. Depolarization block induced with high-affinity ligands in different OSNs.** (**A**) *Or42a* SF larvae tested with sources of 4-hexen-3-one. (**B**) Trajectories recorded for *Or42a* SF larvae for sources (blue disks) of different strengths. (**C**) Attraction of *Or42a* SF larvae to 4-hexen-3-one at a medium-strength source (1:9×10⁴, *n* = 21), but repulsion at a higher-strength source (1:9×10², *n* = 19). (**D**) Top: Mean ± SEM tonic firing rates recorded for *Or42a* OSN (10 nM, *n* = 10; 1 μM, *n* = 10; and 100 μM, *n* = 10). Bottom: Representative voltage traces. Red arrow indicates onset of depolarization block. Raster plot reports the OSN-specific spikes, and the blue bar indicates timing of odor stimulation (**E**) *Or13a* SF larvae tested with sources of pentyl acetate. (**F**) Trajectories recorded for *Or13a* SF larvae for sources (red disks) of different strengths. (**G**) Attraction of *Or13a* SF to pentyl acetate source of medium strength (1:7×10², *n* = 17), but repulsion for high-strength source (1:23, *n* = 16). (**H**) Same as (D) for mean ± SEM tonic firing rates for *Or13a* OSN (1 μM, *n* = 10; 100 μM, *n* = 10; and 10 mM, *n* = 10). (C and G) Statistical comparisons were conducted with Kruskal-Wallis H test, followed by Conover-Iman test (*P < 0.05 upon Bonferroni correction). The bottom row of (B) and (F) shows the probability density functions of distance to source. See data S1 for *P* values.

developed a computational model for the larval *Or42b* OSN that combines a realistic olfactory transduction module (*31*) with a conductance-based neuron model modified to account for the slow inactivation of sodium channels (*28*). The free parameters of the model were optimized to fit the responses of the *Or42b* OSN stimulated by dynamic odor ramps created with a microfluidics system (Fig. 5C and fig. S3A) together with a subset of dose responses elicited by concentrations ranging from subthreshold to high activity yielding depolarization block (Fig. 5D and fig. S3B).

The integrated *Or42b* OSN model recapitulated the dynamical properties of the firing activity of the real OSN (Fig. 5 and figs. S3 and S4). When stimulated with high concentrations of ethyl butyrate (10 μM), the model of the *Or42b* OSN underwent depolarization block (Fig. 5D). The model led to predictions of the firing activity of *Or42b* OSN in excellent quantitative agreement with the experiments for odor steps below and above the threshold for depolarization block (predictions shown as red diamonds; Fig. 5E). In particular, the model accurately predicted sustained firing rate at ~5 μM and the occurrence of depolarization block at 100 μM. In the real *Or42b* OSN, we observed that the latency to the onset of depolarization block decreased as a function of the concentration of the odor stimulation (Fig. 5, F and G). The OSN model accounted for the quantitative relationship observed between the

latency to depolarization block and the stimulus concentration (Fig. 5G). When stimulated by a replay of the concentration time course that elicited behavioral aversion in Fig. 2F, the OSN model entered and exited a depolarization block state with dynamics similar to the real OSN (fig. S4B).

In the framework of dynamical systems theory (*32*), a stable limit cycle corresponds to the neuron firing periodic action potentials, and a stable fixed point corresponds to the absence of action potentials (i.e., depolarization block). To inspect the dynamical properties of the OSN model, we computed the bifurcation diagram shown in Fig. 5B where the concentration of the odor determines the transduction current (Fig. 5A). The bifurcation diagram establishes the existence of a bistable domain of odor concentrations below the so-called saddle node of periodics (SNP) threshold where depolarization block starts. In the bistable domain, the OSN can adopt either a periodic behavior where it fires sustained trains of action potentials or a state of depolarization block. The exact state of the system depends on its history (hysteresis): If the *Or42b* OSN is stimulated by increasing odor concentrations, it will maintain a regime of persistent firing activity until the SNP threshold is passed; by contrast, the *Or42b* OSN can remain in a state of depolarization block, while decreasing odor concentrations can bring the transduction current

**Fig. 5. Development and validation of a computational model reproducing depolarization block in *Or42b* OSN stimulated by ethyl butyrate.** (**A**) Framework of the integrated *Or2b* OSN model accounting for the conversion of an odor stimulus into the generation of action potentials through the cascade of an odorant transduction model, followed by a spike generator model. (**B**) Bifurcation diagram of the *Or42b* OSN model. The spiking regime terminates at the SNP bifurcation. (**C** and **D**) Experimental data (black) used for model fitting (blue) (exponential ramp, $n = 10$; sigmoid ramp, $n = 8$; linear ramp, $n = 10$; 1 μM, $n = 10$; and 10 μM, $n = 9$). (**E**) Dose responses of mean tonic firing rates of real (white circles) and simulated *Or42b* OSN. Blue stars indicate conditions used for model fitting. Red diamonds represent predictions of the model. Sample sizes: 500 pM, $n = 10$; 1 nM, $n = 10$; 5 nM, $n = 10$; 10 nM, $n = 10$; 50 nM, $n = 18$; 100 nM, $n = 18$; 500 nM, $n = 10$; 1 μM, $n = 10$; 5 μM, $n = 8$; 10 μM, $n = 9$; 100 μM, $n = 10$; and 1 mM, $n = 10$. (**F**) Experimental (top) and simulated (bottom) dynamics toward depolarization block for different odor concentrations (blue, 5 μM; orange, 10 μM; green, 100 μM; and red, 1 mM). (**G**) Quantitative relationship between the latency to depolarization and the concentration of the odor simulations for experimental data (white circles) and model predictions (red diamonds). Inset: Box plots of latency to depolarization block for different odor stimulations (Kruskal-Wallis test, followed by Conover-Iman test, $*P < 0.05$). (**H**) Hysteretic nature of *Or42b*-OSN firing rate dynamics in response to a slow linear odor ramp of ethyl butyrate ($n = 9$ recordings). $\phi_{up}$ denotes the concentration where depolarization block arose during the up-gradient phase of the ramp. The cyan arrow highlights the effect of the odor stimulation, which brings the OSN dynamics back to a firing regime (limit cycle).
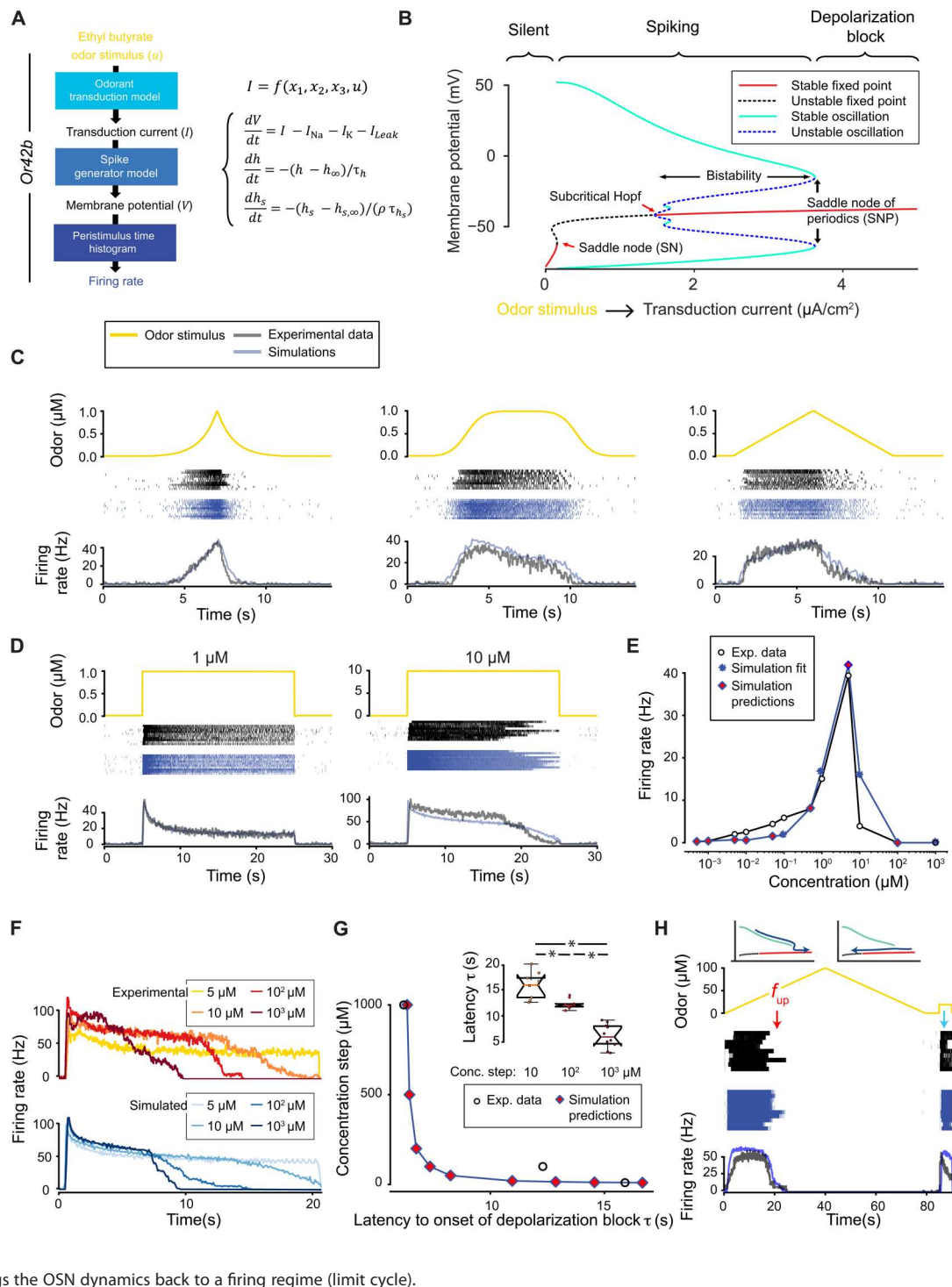


from values higher than the SNP threshold to lower values located within the bistability domain (Fig. 5B).

To experimentally test the existence of the predicted hysteresis in the response of the *Or42b* OSN, we stimulated the real neuron with a slow linear odor ramp ranging from 0 to 100 μM, which encompassed concentrations well below the detection threshold and well above the SNP threshold. On the basis of Fig. 5E, we expected that

the SNP threshold would correspond to a concentration higher than 10 μM. We found that the firing activity of the real *Or42b* OSN increased monotonically up to a threshold value ($\phi_{up} \sim 50$ μM) where it switched to a state of depolarization block. During the down-gradient phase of the odor ramp, the firing activity of the OSN was not restored until the end of the concentration ramp. More specifically, the OSN remained silent for concentrations ranging between $\phi_{up}$

and 0 μM where a strong firing activity was observed during the up-gradient phase of the ramp—a hallmark of hysteretic dynamics.

The history dependence of the OSN response to the slow linear odor ramp was reproduced by the model with remarkable accuracy (Fig. 5H, blue). During the up-gradient phase of the ramp, the OSN model maintained a strong firing activity until the transduction current crossed the SNP threshold and switched from a stable periodic orbit (spiking activity) to a fixed point (depolarization block) (Fig. 5B). Starting with a transduction current above the SNP threshold, the down-gradient phase of the ramp induced a shift of the system's state along the branch of the fixed points, which maintained the state of stable depolarization block—or quasi-stable depolarization block below the subcritical Hopf—while the transduction current decreased to the silent range (Fig. 5B). When the concentration increased again at the end of the ramp, the transduction current returned to a value above the saddle node threshold, which restored the firing activity of the neuron. Following the same logic, hysteresis was observed when the real and simulated $Or42b$ OSNs were stimulated by a series of three concentration steps below and above the SNP threshold that locked the system in a state of depolarization block (fig. S4C).

### Partitioning of the odor concentration by the activity domains of OSNs

The implication of the depolarization block is that high-sensitivity OSNs that are strongly activated at low concentrations of an odor can drop out from the subset of active OSNs at high concentrations of the same odor. To test this hypothesis, we screened published response profiles of larval OSNs (3, 9) to identify pairs of neurons with different sensitivities to the odors studied in Figs. 1, 3, and 4 and compared their respective contribution to chemotaxis across concentration ranges. As illustrated in Fig. 1, ethyl butyrate is a high-affinity ligand of the odorant receptor OR42b (3). By contrast, OR1a has a low affinity for this odor. For strong sources of ethyl butyrate (1:150 and higher) eliciting repulsion in $Or42b$ SF larvae (magenta) compared to wild type (green), $Or1a$ SF larvae (blue) displayed increasingly strong attraction (Fig. 6A and fig. S5A). Consistent with this behavior, the firing activity of the $Or1a$ OSN was higher than baseline at concentrations where $Or42b$ OSN underwent depolarization block (Fig. 6B and fig. S6A). This observation suggested that the ectopic expression of the OR42b odorant receptor in all 21 OSNs should elicit repulsion at high concentrations of ethyl butyrate, while wild-type larvae remained attracted (1:75; Fig. 6A). We confirmed this prediction experimentally (fig. S7).

The same relay principle was applied to the $Or13a$ and $Or42a$ OSNs in response to pentyl acetate. While $Or13a$ SF larvae (orange) were attracted by sources of pentyl acetate at medium strengths ($1:7×10^3$ and $1:7×10^2$), attraction was elicited in $Or42a$ SF larvae (blue) for strong sources (1:70 and higher) that induced repulsion in $Or13a$ SF larvae (Fig. 6C and fig. S5B). In agreement with the behavior, the firing activity of the $Or13a$ OSN underwent depolarization block at high-odor concentrations, while $Or42a$ OSN showed sustained firing activity ($10^4$ μM) (Fig. 6D and fig. S6B). The detection of 4-hexen-3-one involves a sensory sequence of three OSNs to recapitulate the wide range of attraction of wild-type larvae (Fig. 6E and fig. S5, C and D). In response to this odor, $Or42a$ SF larvae (cyan) were attracted by sources at low strength ($1:9×10^4$) but repelled at medium and high strengths ($1:9×10^2$ and higher) for which $Or42b$ SF larvae (magenta) became attracted

(Fig. 6E and fig. S5C). When $Or42b$ SF larvae showed signs of repulsion (1:4), $Or1a$ OSN larvae (blue) showed a stark increase in attraction to the source. The dose responses of the firing activity of $Or42a$, $Or42b$, and $Or1a$ OSNs mirrored this behavioral sequence with $Or42a$ and $Or42b$ OSNs undergoing depolarization block at medium and high concentrations, respectively (Fig. 6F and fig. S6C).

### DISCUSSION

Consistent with the observations that odors activate a subset of OSNs (1–4, 6, 33), the results of Fig. 6 indicate that the sequential recruitment of OSNs with different affinities to the same odor expands the dynamic range of the larval olfactory system. However, contrary to the conventional view, we find that the activity of high-affinity OSNs is not necessarily maintained in the representation of an odor across a wide range of concentrations (Fig. 7). Our observations are likely to generalize beyond the larva because there is growing evidence in the literature that OSNs of adult flies (25, 34), mice (35, 36), and rats (37) undergo depolarization block at high-odor concentrations. Moreover, depolarization block has been observed in response to the gating of ionotropic glutamate receptor (IR) by odorant molecules (25). The pruning of high-affinity OSNs at high-odor concentrations has two implications: First, the same odor might activate distinct subsets of OSNs at low and high concentrations, thereby facilitating central processing and discrimination (Fig. 7, bottom). These differences might explain shifts in the internal percept of an odor across concentrations, leading to the report of drastic changes in the perceived quality of the same odor at low and high concentrations in humans (38, 39). Second, there might be a metabolic advantage in keeping the peripheral representations of odors sparse (40).

In the present work, larvae with an olfactory system restricted to a single type of functional OSNs were all attracted to the odor source at low concentrations. However, the valence of the odor appeared to switch from attractive to aversive behavior at high-odor concentrations (Figs. 1, 3, 4, and 6). In previous work, we have demonstrated that an abrupt decrease in the firing rate of the $Or42a$ OSN below its basal activity level is sufficient to trigger stopping behavior and aversive reorientation responses (21). Here, we showed that all tested OSNs undergo depolarization block at high-odor concentrations (Figs. 2 to 4 and 6). Therefore, we speculate that the change in valence from attraction to repulsion can be explained by a loss of spiking activity in innately attractive OSNs. The aversion caused by the silencing of high-affinity OSNs can be compensated by the activity persisting in other OSNs with lower affinities, as illustrated by the behavior of wild-type larvae (Fig. 6).

While depolarization block has been associated with abnormal neuronal function and disease conditions (41–43), it has been speculated that depolarization block might also contribute to information processing (44, 45). In the mammalian visual system, depolarization block conditions the differential tuning of intrinsically photosensitive retinal ganglion cells to represent light intensity with high efficiency (46). We propose that depolarization block enables the representation of chemosensory stimuli at the sensory periphery over several orders of magnitude of concentration. For instance, it might explain why taste neurons with high sensitivity to sodium shut down at high-salt concentration where low-sensitivity sodium taste neurons become active and natural attraction to
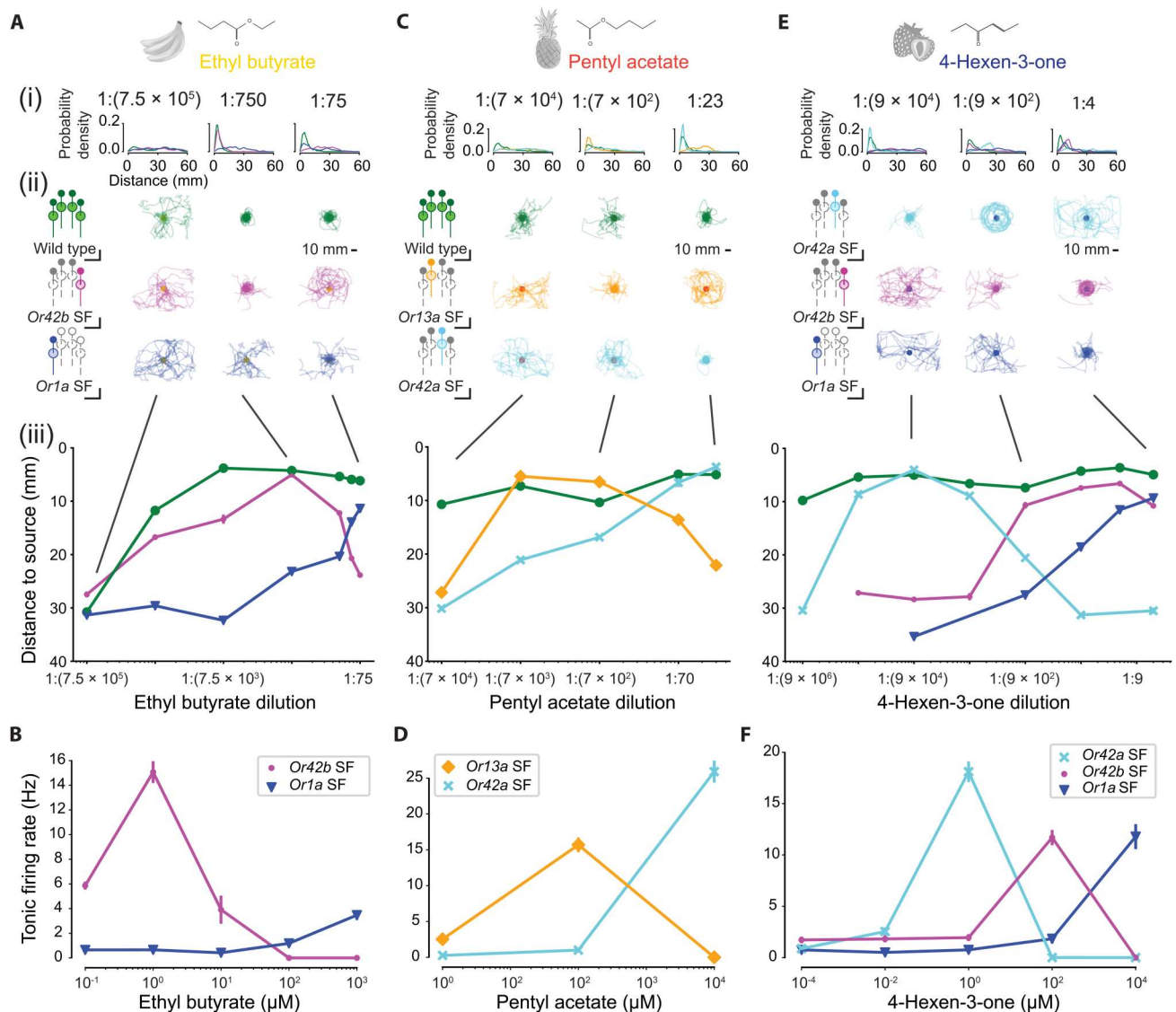
**Fig. 6. Depolarization block maintains sparse odor encoding by tiling the activity domains of OSNs responsive to the same odor.** (**A**) Behavioral response of wild type (green), *Or42b* SF (magenta), and *Or1a* SF (blue) to a series of ethyl butyrate sources of increasingly higher strength. (Ai) Probability density function of distance to source for the trajectories shown in (Aii). (Aiii) While *Or42b* SF is strongly attracted by source of medium strength (1:750), attraction markedly decreases for high-strength source (1:75). By contrast, the attraction level of *Or1a* SF increases monotonically from low- to high-strength sources (mean ± SEM). (**B**) In electrophysiology recordings, *Or42b* OSN enters depolarization block for odor concentrations where *Or1a* OSN shows robust and persistence firing activity. (**C**) Behavioral responses of wild type (green), *Or13a* SF (orange), and *Or42a* SF (cyan) to pentyl acetate sources of increasingly higher strengths. *Or13a* SF displays attraction at medium-strength sources (1:7×10³ to 1:7×10²), but it is repelled at high-strength source (1:70) that produces attraction in *Or42a* SF. (**D**) *Or13a* OSN enters depolarization block for odor concentrations where *Or42a* OSN shows robust and persistent firing activity. (**E**) Behavioral responses of wild type (green), *Or42a* SF (cyan), *Or42b* SF (magenta), and *Or1a* SF (blue) to 4-hexen-3-one sources of increasingly higher strengths. *Or42a* SF is attracted to sources at low strength (1:9×10⁴) but repelled at medium strength (1:9×10²) where *Or42b* SF shows attraction. While *Or42b* SF displays signs of repulsion to a source of very high strength (1:4), *Or1a* SF demonstrates an increase in attraction. (**F**) The *Or42a* and *Or42b* OSNs enter depolarization block at a range that qualitatively matches the behavior shown in (E). The *Or1a* OSN shows robust and persistent firing activity at the highest tested concentration (10 mM). Throughout the figure, firing rates are presented as means ± SEM. See data S1 for sample sizes and *P* values.

sodium switches to repulsion (*47*). Through the recruitment and loss of active sensory neurons, depolarization block creates a previously unknown dimension along which the quality and intensity of a stimulus can be sparsely represented across magnitudes of concentrations (Fig. 7). Hence, depolarization block might be an inherent component of sensory population coding across phyla.

## MATERIALS AND METHODS
### Fly stocks
Larvae were grown at 22°C/60% humidity in 12-hour light/12-hour dark conditions. Throughout the text, *D. melanogaster* "wild type" refers to *w*[1118]. Flies containing the UAS-ChrimsonR transgene (*26*) were raised on fly food containing 0.5 mM all-*trans*-retinal (Sigma-Aldrich, R2500) in the same incubator but protected from light
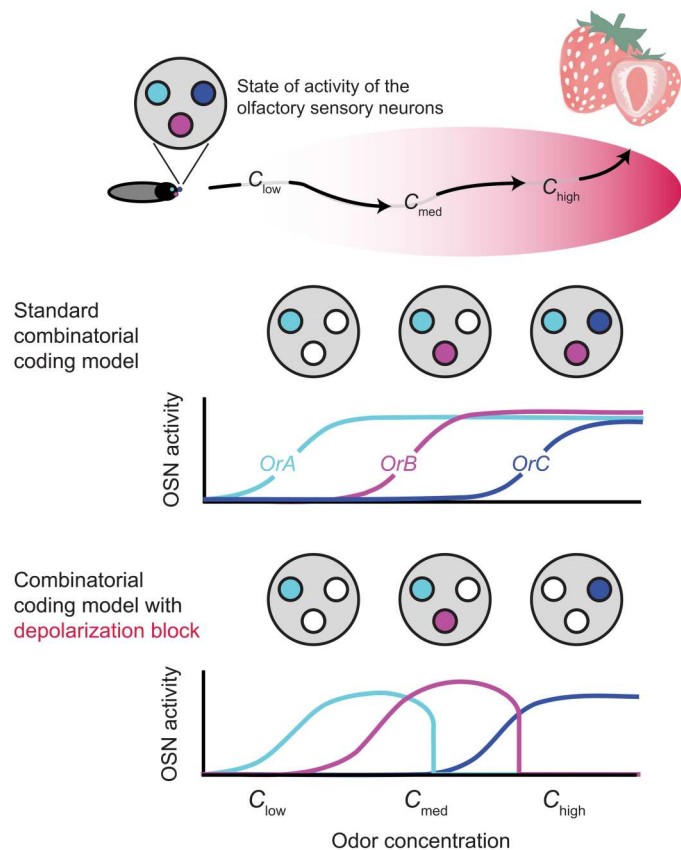
**Fig. 7. Comparison of the standard combinatorial coding model with and without the effects of depolarization block.** (**Top**) While approaching an odor source (strawberry), an animal experiences different concentrations of the odor, depending on its distance to the source. (**Middle**) Representation of different odor concentrations by the peripheral olfactory system assuming a sigmoidal dose-response curve. As the animal approaches the source, an increasing number of OSNs (colored circles) get recruited. (**Bottom**) Our results indicate that depolarization block limits the activity domain of each OSN to a band of concentration, allowing the olfactory code to remain sparser even at high-odor concentrations.

(food vials wrapped in aluminum foil). Ectopic expression of the OR42b receptor was achieved with the UAS-*Or42b* transgene obtained from the cloning of full-length *Or42b* genomic DNA and cloned into the pUAST vector. The full list of transgenic animals is provided in table S1.

## Reagents

Only odors of highest purity were used: ethyl butyrate (Sigma-Aldrich, E15701), pentyl acetate (Sigma-Aldrich, 109584), and 4-hexen-3-one (Sigma-Aldrich, W335207). For ethyl butyrate, the dilution $1:(7.5 \times 10^6)$ corresponds to 1 μM, 1:150 corresponds to 50 mM, and 1:100 corresponds to 75 mM source concentration. For pentyl acetate, $1:(7 \times 10^4)$ corresponds to 100 μM and 1:23 corresponds to 300 mM source concentration. For 4-hexen-3-one, $1:(9 \times 10^6)$ corresponds to 1 μM and 1:4 corresponds to 2 M source concentration.

## Behavior data collection and data analysis

All behavioral experiments were conducted with PiVR (*48*). Throughout the work, animals were tested once (no repeated trials with the same larva). For the data reported in Fig. 1 (A to C), banana fruits were bought in a local supermarket in Santa Barbara, California and allowed to ripen at room temperature (see picture in fig. S1A). For all other behavioral experiments, the odor or virtual reality experiment was conducted according to a published protocol (*17*, *48*). Distance to source was calculated as described before (*48*). Probability density functions were estimated using kernel density estimation.

### Behavior elicited by real banana odor

The behavior apparatus consisted of round petri dishes (Corning Life Sciences, 431760) filled with 1% (w/v) agarose (Genesee Scientific, 20-102) and a custom "fruit cup" (available at https://doi.org/10.25349/D92K69). The fruit cup was 3D–printed (Formlabs, Form 2), washed, and cured as instructed by the manufacturer. Banana odor was allowed to diffuse for 30 s in the experimental setup before a single larva was introduced in the assay at a distance from the source. Larval positions were tracked using PiVR (*48*). Tracking was conducted for up to 4 min. When a larva entered the banana, the experiment ended because the larva had reached its goal and accurate tracking could not be achieved inside the cup with banana.

### Behavior elicited by pure odors

Behavioral experiments involving an odor source were conducted according to a published protocol (*17*, *48*). Briefly, the odor was diluted in paraffin oil (Sigma-Aldrich, 18512-1L) in glass vials with Teflon caps (Neta Scientific, 5182-0556). Odor dilutions were prepared on a daily basis. Agarose [3% (w/v)] was poured on top of lids of 96-well plates (Greiner Bio-One, 656161). A reinforcement ring (Office Depot, 5722) was placed in the center of a different set of 96-well plate lids. Ten microliters of odor (or solvent for controls) was placed inside the reinforcement ring. The lid containing the odor source was placed on top of the lid with the agarose layer. The odor diffused for 30 s in the dish before a single animal was introduced in the arena below the source. Behavior was monitored using PiVR, which performs real-time tracking as described in previous work (*48*). To create virtual odor realities in Fig. 3C, we used a high-powered PiVR setup (*48*). Light intensity was measured using a photodiode (Thorlabs, S130VC) connected to a power meter (Thorlabs, PM100D).

### Behavioral analysis

For consecutive positions of larvae, distance to source was computed with scripts described in (*48*). Briefly, the position of the odor source was defined using the PiVR graphical-user interface. The distance to source was calculated by taking the Euclidian distance between the position of the animal over time and the position of the odor source. To display trajectory plots (e.g., Fig. 1B), individual trajectories were recentered so that the position of the odor source coincided for all trials. The box plots of the banana experiment (Fig. 1C) were calculated on the basis of the median distance to banana measured over 30 s after the tracking had started. Restricting the distance averages to the first 30 s was necessary because many wild-type animals entered the fruit cup after 1 min, thereby ending the experiment. For all odor experiments (e.g., Fig. 1E), we used position data of the first 3 min to calculate the median distance to the source. Kernel density estimation to estimate the probability density

function was performed using a function from the "scipy" library (scipy.stats.gaussian_kde) with standard parameters.

## High-resolution video
Movie S1 was collected with a 100-mm lens (Canon, CA10028LMIS) using side illumination. No tracking was performed for the behavioral sequences illustrated with the high-resolution videos.

## Electrophysiology
Electrophysiological recordings and odor delivery were mainly conducted on the basis of the methodology described in previous work (21).

### Physiological solutions
Electrophysiology was performed according to a methodology described previously (21) with some minor adjustments. Third-instar larvae were washed and placed in ice-cold hemolymph saline (7) (108 mM NaCl, 5 mM KCl, 2 mM CaCl$_2$, 8.2 mM MgCl$_2$, 4 mM NaHCO$_3$, 1 mM NaH$_2$PO$_4$, 5 mM trehalose, 10 mM sucrose, and 5 mM Hepes at pH 7.5). The head was separated from the body in ice-cold saline. The head segment was glued to a coverslip using tissue glue (3M, 084-1469SB). The cuticle dorsal to the larval dorsal organ was removed to make the antennal nerve accessible to the suction electrode. The preparation was immersed in saline in a flow chamber (Harvard Apparatus Inc., 640225) for the entire experiment. The flow chamber was connected to two syringe pumps (World Precision Instruments, Aladdin2-220) for constant perfusion and to ensure smooth flow and evacuation of the odor. The chamber volume was approximately 500 μl. With a flow in the chamber set to 33.3 μl/s, the turnover of the chamber volume was ~15 s.

### Suction electrophysiology setup
Single-barrel recording electrodes (World Precision Instruments, TW150F-3) were pulled (Sutter Instruments, P-87) and flame-polished (ALA Scientific Instruments, CPM-2). The electrode was connected to the head stage (CV-7B, Axon Instruments) of a microelectrode amplifier (Molecular Devices, Axon MultiClamp 700B) with a chlorinated silver wire (Molecular Instruments, 1HLA005). The head stage and suction electrodes were mounted on a motorized micromanipulator (Sutter Instruments, ROE-200 and MPC-200). The antennal nerve was sucked into the recording electrode by manually controlling the strength of external vacuum. The extracellular signal was amplified 100 times at the microelectrode amplifier, digitized (Molecular Devices, Digidata 1550B), and recorded at 10 kHz using the Clampex software (Molecular Devices). The signal was analog-filtered at 10 kHz (Bessel), and 60-Hz main line noise was removed using an adaptive module in the digitizer (HumSilencer, Molecular Devices).

### Odor delivery
At the electrophysiology rig, odor was delivered using a multibarrel glass pipette (World Precision Instruments Inc., 7B100F-4). Pipettes were pulled using a multipipette puller (MicroData Instruments, PMP-107). To benchmark the proper function of the odor pipette, one channel was filled with saline and the other channels were filled with the indicated odor solution diluted in saline and fluorescein (100 ng/μl; Sigma-Aldrich, F6377-100G). An injection needle (Grainger, 5FVK8) was inserted into the back of each barrel of the micropipette. Hot glue was used to achieve an airtight

seal. The channels were then connected to a multichannel pressure controller (Elveflow, model OB1).

The tip of the odor stimulation pipette was placed and maintained directly adjacent to the larval olfactory (dorsal) organ with a micromanipulator (Sutter Instruments, ROE-200 and MPC-200). The distinct geometry of the dorsal organ was identified through the eyepieces of the microscope (Olympus, BX51). To control the amount of odor presented during the experiment, pressure was varied at 50 Hz via a custom Python code (https://doi.org/10.25349/D92K69) in the different channels. As detailed in (21), stimulation flow resulted from the combination of the flow of the odor channel and a channel carrying pure saline. The flow of the saline channel was adjusted to compensate for changes in the flow of the odor channel in such a way that the merged flow remained constant at a value of ~1 nL/s. To control for timing between the different hardware, the digitizer serves as the master clock, while the multichannel pressure controller reports each cycle (at 50 Hz).

### Optogenetic stimulation
A light-emitting diode (LED) emitting red light at a wavelength of 625 nm was used to activate ChrimsonR (Mightex, PLS-0625-030-S). The LED was mounted into the light path of the microscope, which permitted consistent light stimulation between preparation through the 40× water immersion objective. Absolute light intensity at the position of the larval head was estimated using a photodiode (Thorlabs, S170C) connected to a power meter (Thorlabs, PM100D). The absolute light intensity measurements were divided by the area of the field of view of the objective (Olympus, LUMPLFLN 40XW) to obtain the reported microwatts per square millimeter. The LED brightness was adjusted with a LED controller (Mightex, SLA-1200-2), which was in turn controlled by the digitizer, harmonizing time stamps across different stimuli with the recording.

### Semiautomated manual spike sorting
Spike sorting and peristimulus time histogram (PSTH) analysis was performed using custom Python scripts (available at https://doi.org/10.25349/D92K69). While spontaneous activity of OSNs was markedly reduced in the $Orco^{-/-}$ null background, it is not fully abolished (21, 49). Hence, it was necessary to perform spike sorting on all recordings. We developed a spike sorting algorithm (available at https://doi.org/10.25349/D92K69) to aid manual annotation conducted by a trained expert (D.T.). Briefly, the script extracts a vector from features of each waveform (e.g., spike amplitude and spike duration). Uniform Manifold Approximation and Projection (UMAP) is then applied to reduce the dimensionality of the data before hierarchical clustering is performed with the HDSBCAN algorithm (50). Next, the spike cluster of interest is selected. The accuracy of the spike sorter was generally high to identify spikes in odor regimes where the spike waveform does not change considerably during the odor stimulation and required only small corrections by the expert annotator. For recordings where spikes were lost due to depolarization block, it was necessary to manually annotate the portion of the trial where the spike waveform underwent substantial changes. Here, the annotation was guided by the empirical observation that the frequency of spikes remained approximately constant, while the amplitude of the waveform decreased during the period leading to depolarization block.

### Automated FFT spike sorting

Manual spike sorting was complemented by an automated method to identify the onset of depolarization block in electrophysiology recordings. As illustrated in fig. S9, the method relied on a power spectral analysis implemented with a fast Fourier transform (FFT) algorithm. Trains of tonic spikes originating from the OSN could be associated with the frequency with the highest power spectral density. In the automated FFT spike sorting, we applied a sliding time window of 1 s on each recording over which the power spectrum was computed. For each time sample, the firing rate was labeled as the peak nonzero frequency of the signal. To identify the time intervals lacking tonic spiking, a minimum cutoff value in the peak power spectral density was applied to classify whether sustained neural activity was present. For each recording, this cutoff value was defined as the 95th percentile of power spectral values such that peak spectral densities above this threshold were classified as spiking activity and peak spectral densities below this threshold are filtered out as background noise. To validate the accuracy of the automated FFT spike sorting algorithm to identify the termination of tonic spiking at the onset of depolarization block, we used a set of recordings that had been manually annotated as ground truth (fig. S9B).

### Analysis of electrophysiology data

PSTHs were calculated as previously described (21). Briefly, each spike was convolved with a Gaussian filter. Spikes were then grouped in 33-ms bins and averaged across experiments to yield the mean PSTH. Last, a Gaussian filter was applied to smoothen the signal. For the quantification of the firing rate of the dose responses, the phasic response to the odor stimulus was computed as the mean firing rate over the first 2 s after stimulus onset. The tonic response was defined as the mean over the last 2 s of the 20-s stimulus.

### Statistical analysis

No statistical methods were used to systematically predetermine the sample size of each experimental condition, but a preliminary behavioral screen had shown that a sample size of 15 was sufficient to reliably establish the repulsive behavior of Or42b SF larvae at a source dilution of 1:150 of ethyl butyrate. Therefore, we used a sample size of 15 trials as a target for the rest of the work. In addition, we verified that the final sample sizes used in the study were adequate to ensure a sufficiently large effect size for all statistical tests (data S1). Custom-written Python scripts were written to create the plots and calculate statistics (https://doi.org/10.25349/D92K69). To establish whether parametric statistical tests could be used, we always tested for equality of variance using Levene's test (scipy.stats.levene with standard settings) and for normality using Lilliefors' test (statsmodels.stats.diagnostic.lilliefors with standard settings). For multiple comparisons, we used either analysis of variance (ANOVA) (scipy.stats.f_oneway) or the nonparametric Kruskal-Wallis test (scipy.stats.kruskal with standard settings), followed by Conover-Iman test (scikit_posthocs.posthoc_conover with standard settings). For pairwise comparison, we used the t test (scipy.stats.ttest_ind with standard settings) if normality and equality of variance assumptions for parametric tests was satisfied (see above). If a nonparametric test had to be used, we used the Wilcoxon rank sum test (scipy.stats.ranksums with standard settings). All statistical tests were two-sided. For each figure panel, Bonferroni multiple-test correction was used. Effect sizes were adapted to the statistical test under consideration (51). For parametric pairwise tests, Cohen's d was calculated as explained in (51). Throughout the article, box plots represent the following elements: Center line indicates the median. Box extends from the first quartile (Q1) to the third quartile (Q3). The whiskers extend to Q1 and Q1.5 interquartile range (IQR) and Q3 + 1.5 IQR. The notch indicates the confidence interval around the median. All data points, including outliers, are plotted.

### Data exclusion procedure

All collected behavioral data are shown in the figures of the manuscript. The electrophysiology recordings were subject to several sources of variability that could not be fully controlled during data collection. Infrequent head movements due to the sporadic twitching of pharyngeal muscles were consequential as they could result in a transient misalignment of the head with the odor stream. While these rare events did not produce any noticeable effects on recordings involving odor concentrations below the depolarization threshold (e.g., Figs. 2E and 5C), they were occasionally found to alter recordings featuring depolarization block during longer (>30 s) trials (Figs. 2F and 5H and fig. S4, B and C). We speculate that head movements could produce abrupt drops of odor concentration that were sufficient to push the neuron out of the depolarization block regime. This prediction is based on the simulations with the computational model presented in Fig. 5B. To identify problematic trials, we screened the recordings with the following fixed set of criteria that we associated with potential artifacts: (i) sudden changes in local field potential indicative of head movements and (ii) delayed or nonexistent response during a control odor step stimulus elicited at the end of the recording. The first criterion aimed to identify transient misalignments of odor pipette with the head, while the second aimed to identify permanent misalignments. These criterions were established after collecting preliminary datasets and before collecting datasets shown here.

### OSN model

The OSN model was inspired by the work of (28, 31). Like in the cascade model of (31), the initial conversion of the odor detection into firing activity is viewed as a cascade of an odorant transduction process and a biophysical spike generator. However, while the biophysical spike generator is modeled as a Connor-Stevens point neuron in (31), we instead adopt an alternative model (28) to include the characteristics of depolarization block in regimes of high-intensity stimulation. Custom-written MATLAB code is available at https://doi.org/10.25349/D92K69.

### Odor transduction model

We adapted the biophysical cascade model (31) of odor transduction from the adult fly to the larva. Besides the reoptimization of several parameters for the specific odorant-receptor pair in our assay (ethyl butyrate, OR42b), no modifications to the equations were required to reproduce the firing responses in the larval Or42b OSN. The model proposes the division of the olfactory transduction process into several mechanisms: (i) the peri-receptor process, (ii) odorant receptor binding, and (iii) co-receptor channel gating. Collectively, this signal cascade converts an odor concentration into a transduction current mediated by the opening of the co-receptor ORCO (52).

The peri-receptor process, which models the diffusion and absorption of odorant molecules by the odorant receptor, is described

as follows as an odorant concentration profile at the odorant receptor $v$

$$v = \int h(t-s)\, u(s)\, ds + \gamma \int h(t-s)\, du(s) \quad (1)$$

where $u$ is the temporal waveform of the odor concentration experienced by the larva (fig. S8, C and E), $h(t)$ is a low-pass linear filter, and $\gamma$ is a weighting factor that determines the dependency of the filtered waveform $v$ on the odor concentration $u$ and the odor gradient $du/dt$. The output odorant concentration profile $v$ then interacts with the "private" odorant receptors (OR42b). This mechanism underlying this interaction is named as the bound-receptor generator, which models the fraction of odorant receptors $x_1$ that are bound at any given time

$$\frac{dx_1}{dt} = b_r\, v\, (1 - x_1) - d_r\, x_1 \quad (2)$$

with the assumption that each private receptor only exists in one of two states: bound or unbound. The equilibrium fraction of bound odorant receptors is driven by the odorant concentration profile $v$, with the parameters $b_r$ defining the binding rate and $d_r$ representing the dissociation rate. The fraction of bound odorant receptors $x_1$ then modulates the opening of the co-receptor channel and calcium channel, modeled by gating variables $x_2$ and $x_3$, respectively

$$\frac{dx_2}{dt} = \alpha_2\, x_1(1 - x_2) - \beta_2\, x_2 - \kappa\, x_2^{2/3}\, x_3^{2/3}$$
$$\frac{dx_3}{dt} = \alpha_3\, x_2 - \beta_3 x_3 \quad (3)$$

In Eq. 3, the gating variable $x_2$ represents the opening of the ion channel gated by the co-receptor ORCO (52). The opening of the co-receptor is promoted by the odorant binding variable $x_1$, which interacts with the gating variable $x_3$ through a feedback loop involving a calcium channel (31). The inhibitory term $\kappa\, x_2^{2/3}\, x_3^{2/3}$ models the calcium feedback with $\kappa$ as a constant. Last, the parameters $\alpha_2$, $\beta_2$ define the rate of increase and decrease of ORCO gating $x_2$, while $\alpha_3$, $\beta_3$ represent the rate of increase and decrease of calcium gated by $x_3$. Together, the transduction current $I$ resulting from this odorant transduction processed is given as a Hill function of the co-receptor gating variable $x_2$

$$I = \frac{I_{\max}\, x_2}{x_2 + c^p} \quad (4)$$

where $I_{\max}$ defines the maximum transduction current that can result through the co-receptor channel. The parameters $c$ and $p$ define the half-activation coefficient and Hill coefficient of the co-receptor channel, respectively. The different steps of the transduction cascade are illustrated in fig. S8C for an odor ramp featuring a linear increase in odor concentration interrupted by a gap.

### Spike generator model
In the biophysical cascade model (31), the Connor-Stevens model was used to simulate the transformation of transduction current into biological spikes. Here, we adopt the framework of the Qian 3D model (28), which was proposed to describe depolarization block in midbrain dopamine neurons. Like the original Hodgkin-Huxley model (53), the formulation of Qian *et al.* (28) is a single-compartment neuron model with three currents: fast sodium $I_{\mathrm{Na}}$,

delayed rectifier potassium $I_K$, and a leak current $I_{\mathrm{leak}}$

$$I_{\mathrm{Na}} = g_{\mathrm{Na}}\, m^3\, h\, h_s (V - E_{\mathrm{Na}})$$
$$I_K = g_K\, n^3\, (V - E_K) \quad (5)$$
$$I_{\mathrm{leak}} = g_{\mathrm{leak}}\, (V - E_{\mathrm{leak}})$$

In the above equations, $E_{\mathrm{Na}}$, $E_K$, and $E_{\mathrm{leak}}$ are the respective Nernst potentials of each channel. $g_{\mathrm{Na}}$, $g_K$, and $g_{\mathrm{leak}}$ are parameters modeling the maximal conductance per unit area of each channel. Symbols $n$, $m$, $h$, and $h_s$ are dimensionless state variables mediating the gating of the three currents, modeled as time-dependent functions of the membrane potential $V$. For simplicity, the gating variable for sodium activation ($m$) is set to its steady-state value as it is significantly faster than the other gating variables, while the gating variable for potassium activation ($n$) is dynamically yoked to the time scale of the gating variable $h$ (28). Thus, the Qian 3D model contains three state variables: $V$, $h$, and $h_s$. The feature of the Qian 3D model that distinguishes this work from other models is the distinction between fast inactivation ($h$) and slow inactivation ($h_s$) in the sodium current as a mechanism for explaining the dynamics of depolarization block. The Qian 3D model consists of the following system of ordinary differential equations

$$\frac{dV}{dt} = I - I_{\mathrm{Na}} - I_K - I_{\mathrm{leak}}$$
$$\frac{dh}{dt} = -(h - h_\infty)/\tau_h \quad (6)$$
$$\frac{dh_s}{dt} = -(h_s - h_{s,\infty})/(\rho \tau_{h_s})$$

where $h_\infty$ and $h_{s,\infty}$ are voltage-dependent steady-state values of the fast and slow inactivation variables associated with the sodium channels. Variables $\tau_h$ and $\tau_{h_s}$ are voltage-dependent time constants that modulate the rate of inactivation (the parameters and exact definitions of each gating variable can be found in table S4). Together, these variables determine the rate at which the spike amplitude and frequency changes during depolarization block. In particular, the scaling parameter $\rho$ of the time constant $\tau_{h_s}$ modulates the duration for which spiking continues upon the onset of depolarization block. The dynamics of the variables of the spike generator model is illustrated in fig. S8 (D and F) for two representative odor stimuli.

### Variability and noise in the spiking activity of the Or42b OSN
As illustrated by the bifurcation diagram of the OSN model in Fig. 5B, the OSN is silent when unstimulated. However, we observe experimentally that basal activity is present on the order of 1 to 5 Hz even when no olfactory signal is present (fig. S8A), which is consistent with previous observations (21, 24, 49, 54–56). To replicate the basal firing rate of the OSN in the absence of odor stimulation, we assume that noise affects the olfactory transduction cascade model of the OSN. We model this by injecting Gaussian noise $\varepsilon \sim N(0, \sigma)$ at the level of the transduction current to simulate basal activity of the OSN in the absence of olfactory input such that $I \to I + \varepsilon$. The value of the basal noise $\sigma$ is modeled by fitting the distribution of firing rates that are observed in the OSN in the absence of odor, by finding $\sigma$ that minimizes the Kullback-Leibler divergence between recorded and simulated firing rate distributions (as shown in fig. S8A).

In addition, we noted the existence of variability in the sensitivity to odor across experimental trials. This was particularly apparent in

conditions displaying depolarization block, as we observed that the OSNs of each animal were firing or silent over different time intervals (figs. S3, B and C, and S4B). As the variability in OSN responses could not be reproduced with basal noise alone and may be due to variability in olfactory sensitivity across animals, we also assume that each OSN trial we simulate differs slightly in its model parameters. We model this effect by adding uncertainty to the maximum transduction current $I_{max}$ of the OSN in each simulated trial such that $I_{max} \rightarrow I_{max}(1 + \delta_I)$, where $\delta_I \sim N(0, 0.1)$ is a normally distributed random variable. We empirically found that this variability accounted for the sequential onset of depolarization block observed across different experimental trials, such as for 10 μM step stimulus of ethyl butyrate (Fig. 5D).

### Optimization of the parameters of the model

The parameters of the OSN model were fit on a subset of data from electrophysiology recordings. For each condition, the error was defined as the normalized root mean square error (NRMSE) between the recorded firing rate and predicted firing rate of the model (table S2). The objective function was the mean error of all conditions in the training set. All parameters were optimized using global optimization toolbox of MATLAB. In the parameter optimization procedure, we matched the number of simulated trials with the existing number of experimental trials. The full list of optimized parameters of the odor transduction model can be found in table S3, and the optimized parameters of the spike generator model can be found in table S4. The results are shown in Fig. 5 and figs. S3, S4, and S8.

### Physical model for odor diffusion

To quantify the sensory experience of larvae in the rectangular arena at different source concentrations of ethyl butyrate (Fig. 1, E and F), we modeled the diffusion of odor from the reinforcement ring on the lid to the surrounding air (fig. S10). As in previous work (21), the odor gradient was found to be dynamic with an initial period of diffusion from the source center, followed by a gradual depletion of the source. To predict the odor gradient perceived by larvae within the behavioral arena for different source concentrations, we used a generalized version of the physical 3D diffusion model developed in (21). The simulations of the odor diffusion model were conducted with the partial differential equation toolbox of MATLAB, using an arena geometry generated and imported from an open-source computer-aided design (CAD) software OpenSCAD (57).

### Diffusion equation and model geometry

The diffusion processes of the odor within the air and within the droplet are modeled as a diffusion process

$$\frac{\partial z}{\partial t} = D_i \nabla^2 z \tag{7}$$

where $D_i$ denotes the diffusion constant for either air, $D_{air}$, or the droplet, $D_{drop}$. A flux continuity condition is applied at the droplet-air boundary on the surface of the droplet. The base of the droplet in contact with the top surface of the arena is modeled as a no-flux boundary. For the interaction of the odor with the plastic surfaces and the agarose surfaces of the arena, we followed the approach described in (21) and modeled the

adsorption of odor on these surfaces as Robin boundary conditions

$$\text{Plastic boundary}: -\overrightarrow{n} \cdot \overrightarrow{J} = k_{plastic}(z_{0,plastic} - z)$$
$$\text{Agarose boundary}: -\overrightarrow{n} \cdot \overrightarrow{J} = k_{agar}(z_{0,agar} - z) \tag{8}$$

where $\overrightarrow{n}$ is the unit vector in the direction normal to the boundary under consideration. Parameters $k_{plastic}$ and $k_{agar}$ are the reaction rates. $z_{0, plastic}$ and $z_{0, agar}$ are the saturation concentrations of the odorant on the boundary. This boundary condition assumes that desorption at the boundary occurs if the concentration of the odorant in air is less than the saturation concentration, with the boundary acting as an odor source. On the other hand, a higher concentration of the odorant in air would lead to adsorption at the boundary, with the boundary functioning as an odor sink. We noted, however, that the source concentrations of ethyl butyrate used in some experiments of this study were orders of magnitude smaller than those used in (27). As a result, the assumption that the plastic and agarose surfaces of the arena act as source terms may not be valid at low source concentrations. In our implementation of the physical 3D diffusion model, we therefore added a conditional statement to the boundary conditions to account for regions of the arena where saturation at the boundary does not occur

$$\text{Plastic boundary}: \text{If } z < z_{0,plastic}, -\overrightarrow{n} \cdot \overrightarrow{J} = 0$$
$$\text{Agarose boundary}: \text{If } z < z_{0,agarose}, -\overrightarrow{n} \cdot \overrightarrow{J} = 0 \tag{9}$$

The geometry of the experimental arena is shown in fig. S10A. The rectangular arena has a width of 8.5 cm and a length of 12.7 cm. The height of the arena from the lid to the base of the agarose surface is 0.7 cm. The geometry of the droplet on the lid can be viewed as an inverted half sphere hanging from the top surface of the arena. For simulation purposes, we approximated the droplet as a cone, with a radius of $r_{drop}$=0.3 cm with a height of $h_{drop}$=0.1 cm. The droplet therefore has a volume of $V_{drop} = \frac{\pi}{3} r_{drop}^2 h_{drop} \approx 10$ μl. We assume that the initial odorant concentration in the air is zero, while the initial odorant concentration in the droplet is equivalent to the applied source concentration. Thus, the flux of odor at the droplet-air boundary is proportional to the applied source concentration. In each simulation, the odorant diffuses from the droplet into the air over a duration of 30 s before each animal is introduced into the arena.

The parameters of the model were fit to match measurements made by Fourier transform-infrared spectroscopy (FT-IR) (17). To capture the evolution of the shape and magnitude of the odor profile, these measurements were made at different cross sections of the arena at different time intervals. To guide the parameter optimization, we used data for ethyl butyrate in an identical arena recorded from a previous study (27), at source concentrations of 1:30 and 1:15. Parameter optimization was performed using the global optimization toolbox of MATLAB by minimizing the NRMSE between the simulated odor concentration to FT-IR spectroscopy measurements. After parameter optimization, we then validated the model with FT-IR measurements recorded at source dilutions of 1:(7.5 × 10³), 1:750, 1:75, and 1:30 along the center cross section of the arena (fig. S10D). The 3D diffusion model was found to scale well across orders of magnitude in the source

concentration. Parameters of the computation model for 3D odor diffusion can be found in table S5.

### Correlating odor concentrations in behavioral arrays and at the electrophysiology rig

In the behavioral experiments, animals are exposed to the odor in gaseous phase. The electrophysiology data were collected upon odor stimulation in liquid phase (saline) due to the immersion of the head preparation in saline. To correlate the concentration of the odor in gaseous phase with the concentration of odor in liquid phase, we identified the lowest amount of odor that animals were able to detect in the behavioral experiment (source dilution of 1:150,000) and used our simulations of the odor diffusion (see above) to calculate the average amount of odor in the air. By taking the median odor concentration in the air at a source dilution of 1:150,000, we find the odor concentration to be ~2.9 nM. At the electrophysiology rig, the lowest odor concentration in the odor pipette where we found spikes in response to the odor stimulus was $10^{-8}$ M. We made the assumption that the lowest concentration at which the spikes were observed in the electrophysiology recordings with waterborne odor stimulation corresponded to the lowest concentration at which odor attraction was observed to airborne odor stimulation in the behavioral arena. Following this logic, the liquid to air conversion rate was calculated as being 10 nM/2.9 nM = 3.4. Combined with the simulations of the time courses of the odor concentration experienced during behavior, this conversion factor was used to prepare the stimulus profiles of the trajectory replays shown in Fig. 2 (E and F) and figs. S1 (I and J), S3A, and S4 (A and B).

## Supplementary Materials

**This PDF file includes:**
Figs. S1 to S10
Tables S1 to S5
References

**Other Supplementary Material for this manuscript includes the following:**
Movie S1
Data S1

## REFERENCES AND NOTES

1. B. Malnic, J. Hirono, T. Sato, L. B. Buck, Combinatorial receptor codes for odors. *Cell* **96**, 713–723 (1999).
2. E. A. Hallem, J. R. Carlson, Coding of odors by a receptor repertoire. *Cell* **125**, 143–160 (2006).
3. S. A. Kreher, D. Mathew, J. Kim, J. R. Carlson, Translation of sensory input into behavioral output via an olfactory system. *Neuron* **59**, 110–124 (2008).
4. M. Meister, T. Bonhoeffer, Tuning and topography in an odor map on the rat olfactory bulb. *J. Neurosci.* **21**, 1351–1360 (2001).
5. B. D. Rubin, L. C. Katz, Optical imaging of odorant representations in the mammalian olfactory bulb. *Neuron* **23**, 499–511 (1999).
6. M. Wachowiak, L. B. Cohen, Representation of odorants by receptor neuron input to the mouse olfactory bulb. *Neuron* **32**, 723–735 (2001).
7. J. W. Wang, A. M. Wong, J. Flores, L. B. Vosshall, R. Axel, Two-photon calcium imaging reveals an odor-evoked map of activity in the fly brain. *Cell* **112**, 271–282 (2003).
8. S. Firestein, Physiology of transduction in the single olfactory sensory neuron. *Soc. Gen. Physiol. Ser.* **47**, 61–71 (1992).
9. G. Si, J. K. Kanwal, Y. Hu, C. J. Tabone, J. Baron, M. Berck, G. Vignoud, A. D. T. Samuel, Structured odorant response patterns across a complete olfactory receptor neuron population. *Neuron* **101**, 950–962.e7 (2019).
10. J. Reisert, H. R. Matthews, Response properties of isolated mouse olfactory receptor cells. *J. Physiol.* **530**, 113–122 (2001).
11. R. I. Wilson, Z. F. Mainen, Early events in olfactory processing. *Annu. Rev. Neurosci.* **29**, 163–201 (2006).
12. O. J. Ahmed, M. A. Kramer, W. Truccolo, J. S. Naftulin, N. S. Potter, E. N. Eskandar, G. R. Cosgrove, A. S. Blum, L. R. Hochberg, S. S. Cash, Inhibitory single neuron control of seizures and epileptic traveling waves in humans. *BMC Neurosci.* **15**, F3 (2014).
13. C. J. Marcuccilli, A. K. Tryba, W. van Drongelen, H. Koch, J. C. Viemari, F. Peña-Ortega, E. L. Doren, P. Pytel, M. Chevalier, A. Mrejeru, M. H. Kohrman, R. E. Lasky, S. M. Lew, D. M. Frim, J.-M. Ramirez, Neuronal bursting properties in focal and parafocal regions in pediatric neocortical epilepsy stratified by histology. *J. Clin. Neurophysiol.* **27**, 387–397 (2010).
14. J. P. Dreier, C. Reiffurth, J. Woitzik, J. A. Hartings, C. Drenckhahn, C. Windler, A. Friedman, B. MacVicar, O. Herreras; COSBID study group, How spreading depolarization can be the pathophysiological correlate of both migraine aura and stroke. *Acta Neurochir. Suppl.* **120**, 137–140 (2014).
15. H. K. M. Dweck, S. A. M. Ebrahim, T. Retzke, V. Grabe, J. Weißflog, A. Svatoš, B. S. Hansson, M. Knaden, The olfactory logic behind fruit odor preferences in larval and adult *Drosophila*. *Cell Rep.* **23**, 2524–2531 (2018).
16. M. Cobb, What and how do maggots smell? *Biol. Rev.* **74**, 425–459 (1999).
17. M. Louis, T. Huber, R. Benton, T. P. Sakmar, L. B. Vosshall, Bilateral olfactory sensory input enhances chemotaxis behavior. *Nat. Neurosci.* **11**, 187–199 (2008).
18. P. Monte, C. Woodard, R. Ayer, M. Lilly, H. Sun, J. Carlson, Characterization of the larval olfactory response in *Drosophila* and its genetic basis. *Behav. Genet.* **19**, 267–283 (1989).
19. E. O. Aceves-Piña, W. G. Quinn, Learning in normal and mutant *Drosophila* larvae. *Science* **206**, 93–96 (1979).
20. E. Fishilevich, A. I. Domingos, K. Asahina, F. Naef, L. B. Vosshall, M. Louis, Chemotaxis behavior mediated by single larval olfactory neurons in *Drosophila*. *Curr. Biol.* **15**, 2086–2096 (2005).
21. A. Schulze, A. Gomez-Marin, V. G. Rajendran, G. Lott, M. Musy, P. Ahammad, A. Deogade, J. Sharpe, J. Riedl, D. Jarriault, E. T. Trautman, C. Werner, M. Venkadesan, S. Druckmann, V. Jayaraman, M. Louis, Dynamical feature extraction at the sensory periphery guides chemotaxis. *eLife* **4**, e06694 (2015).
22. M. J. Jordán, K. Tandon, P. E. Shaw, K. L. Goodner, Aromatic profile of aqueous banana essence and banana fruit by gas chromatography−mass spectrometry (GC-MS) and gas chromatography−olfactometry (GC-O). *J. Agr. Food Chem.* **49**, 4813–4817 (2001).
23. S. T. Sweeney, K. Broadie, J. Keane, H. Niemann, C. J. O'Kane, Targeted expression of tetanus toxin light chain in *Drosophila* specifically eliminates synaptic transmission and causes behavioral defects. *Neuron* **14**, 341–351 (1995).
24. K. I. Nagel, R. I. Wilson, Biophysical mechanisms underlying olfactory receptor neuron dynamics. *Nat. Neurosci.* **14**, 208–216 (2011).
25. L.-H. Cao, B.-Y. Jing, D. Yang, X. Zeng, Y. Shen, Y. Tu, D.-G. Luo, Distinct signaling of *Drosophila* chemoreceptors in olfactory sensory neurons. *Proc. Natl. Acad. Sci. U.S.A.* **113**, E902–E911 (2016).
26. N. C. Klapoetke, Y. Murata, S. S. Kim, S. R. Pulver, A. Birdsey-Benson, Y. K. Cho, T. K. Morimoto, A. S. Chuong, E. J. Carpenter, Z. Tian, J. Wang, Y. Xie, Z. Yan, Y. Zhang, B. Y. Chow, B. Surek, M. Melkonian, V. Jayaraman, M. Constantine-Paton, G. K.-S. Wong, E. S. Boyden, Independent optical excitation of distinct neural populations. *Nat. Methods* **11**, 338–346 (2014).
27. K. Asahina, M. Louis, S. Piccinotti, L. B. Vosshall, A circuit supporting concentration-invariant odor perception in *Drosophila*. *J. Biol.* **8**, 9 (2009).
28. K. Qian, N. Yu, K. R. Tucker, E. S. Levitan, C. C. Canavier, Mathematical analysis of depolarization block mediated by slow inactivation of fast sodium channels in midbrain dopamine neurons. *J. Neurophysiol.* **112**, 2779–2790 (2014).
29. C.-S. Hong, B. Ganetzky, Molecular characterization of neurally expressing genes in the para sodium channel gene cluster of *Drosophila*. *Genetics* **142**, 879–892 (1996).
30. W.-H. Lin, C. Günay, R. Marley, A. A. Prinz, R. A. Baines, Activity-dependent alternative splicing increases persistent sodium current and promotes seizure. *J. Neurosci.* **32**, 7267–7277 (2012).
31. A. A. Lazar, C.-H. Yeh, A molecular odorant transduction model and the complexity of spatio-temporal encoding in the *Drosophila* antenna. *PLOS Comput. Biol.* **16**, e1007751 (2020).
32. S. H. Strogatz, *Nonlinear Dynamics and Chaos* (CRC Press, 2018).
33. D. Münch, C. G. Galizia, DoOR 2.0—Comprehensive mapping of *Drosophila* melanogaster odorant responses. *Sci. Rep.* **6**, 21841 (2016).
34. F. Martin, E. Alcorta, Measuring activity in olfactory receptor neurons in *Drosophila*: Focus on spike amplitude. *J. Insect Physiol.* **95**, 23–41 (2016).
35. G. Sicard, Electrophysiological recordings from olfactory receptor cells in adult mice. *Brain Res.* **397**, 405–408 (1986).

36. T. Connelly, A. Savigner, M. Ma, Spontaneous and sensory-evoked activity in mouse olfactory sensory neurons with defined odorant receptors. *J. Neurophysiol.* **110**, 55–62 (2013).

37. P. Duchamp-Viret, A. Duchamp, M. A. Chaput, Peripheral odor coding in the rat and frog: Quality and intensity specification. *J. Neurosci.* **20**, 2383–2390 (2000).

38. R. Gross-Isseroff, D. Lancet, Concentration-dependent changes of perceived odor quality. *Chem. Senses* **13**, 191–204 (1988).

39. D. G. Laing, P. K. Legha, A. L. Jinks, I. Hutchinson, Relationship between molecular structure, concentration and odor qualities of oxygenated aliphatic molecules. *Chem. Senses* **28**, 57–69 (2003).

40. S. B. Laughlin, R. R. de Ruyter van Steveninck, J. C. Anderson, The metabolic cost of neural information. *Nat. Neurosci.* **1**, 36–41 (1998).

41. A. Călin, A. S. Ilie, C. J. Akerman, Disrupting epileptiform activity by preventing parvalbumin interneuron depolarization block. *J. Neurosci.* **41**, 9452–9465 (2021).

42. A. Bragin, M. Penttonen, G. Buzsáki, Termination of epileptic afterdischarge in the hippocampus. *J. Neurosci.* **17**, 2567–2579 (1997).

43. K. E. Houssaini, C. Bernard, V. K. Jirsa, The epileptor model: A systematic mathematical analysis linked to the dynamics of seizures, refractory status epilepticus, and depolarization block. *Eneuro* **7**, (2020).

44. A. Dovzhenok, A. S. Kuznetsov, Exploring neuronal bistability at the depolarization block. *PLOS ONE* **7**, e42811 (2012).

45. E. Marder, L. F. Abbott, G. G. Turrigiano, Z. Liu, J. Golowasch, Memory from the dynamics of intrinsic membrane currents. *Proc. Natl. Acad. Sci. U.S.A.* **93**, 13481–13486 (1996).

46. E. S. Milner, M. T. H. Do, A population representation of absolute light intensity in the mammalian retina. *Cell* **171**, 865–876.e16 (2017).

47. Y. V. Zhang, J. Ni, C. Montell, The molecular basis for attractive salt-taste coding in *Drosophila*. *Science* **340**, 1334–1338 (2013).

48. D. Tadres, M. Louis, PiVR: An affordable and versatile closed-loop platform to study unrestrained sensorimotor behavior. *PLOS Biol.* **18**, e3000712 (2020).

49. D. J. Hoare, C. R. McCrohan, M. Cobb, Precise and fuzzy coding by olfactory sensory neurons. *J. Neurosci.* **28**, 9710–9722 (2008).

50. R. J. G. B. Campello, D. Moulavi, J. Sander, Density-based clustering based on hierarchical density estimates, in *Pacific-Asia Conference on Knowledge Discovery and Data Mining* (Springer, 2013), pp. 160–172.

51. M. Tomczak, E. Tomczak, The need to report effect size estimates revisited. An overview of some recommended measures of effect size. *Trends Sport Sci.* **1**, 19–25 (2014).

52. M. C. Larsson, A. I. Domingos, W. D. Jones, M. E. Chiappe, H. Amrein, L. B. Vosshall, Or83b encodes a broadly expressed odorant receptor essential for *Drosophila* olfaction. *Neuron* **43**, 703–714 (2004).

53. A. L. Hodgkin, A. F. Huxley, A quantitative description of membrane current and its application to conduction and excitation in nerve. *J. Physiol.* **117**, 500–544 (1952).

54. M. de Bruyne, K. Foster, J. R. Carlson, Odor coding in the *Drosophila* antenna. *Neuron* **30**, 537–552 (2001).

55. A. A. Dobritsa, W. van der Goes van Naters, C. G. Warr, R. A. Steinbrecht, J. R. Carlson, Integrating the molecular and cellular basis of odor coding in the *Drosophila* antenna. *Neuron* **37**, 827–841 (2003).

56. E. A. Hallem, M. G. Ho, J. R. Carlson, The molecular basis of odor coding in the *Drosophila* antenna. *Cell* **117**, 965–979 (2004).

57. M. Kintel, C. Wolf, OpenSCAD (2014);http://files.openscad.org/mm.pdf.

58. R. Benton, K. S. Vannice, C. Gomez-Diaz, L. B. Vosshall, Variant ionotropic glutamate receptors as chemosensory receptors in *Drosophila*. *Cell* **136**, 149–162 (2009).

59. J. Eliason, A. Afify, C. Potter, I. Matsumura, A GAL80 collection to inhibit GAL4 transgenes in *Drosophila* olfactory sensory neurons. *G3 (Bethesda)* **8**, 3661–3668 (2018).